Journal of the Brazilian Society of Mechanical Sciences and Engineering (2018) 40:42
https://doi.org/10.1007/s40430-017-0935-1

TECHNICAL PAPER

Investigation of heat transfer and pressure drop of turbulent flow in tubes with successive alternating wall deformation under constant wall temperature boundary conditions

Hasan Najafi Khaboshan[1] · Hamid Reza Nazif[1]

Received: 8 September 2017 / Accepted: 28 November 2017 / Published online: 17 January 2018
© The Brazilian Society of Mechanical Sciences and Engineering 2018

Abstract

In this study, the effects of the presence of multi-longitudinal vortex and various rotation angles between the pitches of alternating elliptical axis (AEA) tubes on heat transfer and pressure drop of turbulent flow were numerically investigated. Turbulent flow of water fluid was simulated at Reynolds numbers of 10,000–60,000. The turbulent flow and heat transfer in the tubes were discussed in terms of parameters such as static pressure, velocity magnitude, wall shear stress, turbulent intensity, performance evaluation criterion and the field synergy principle. The results demonstrate that most heat transfer occurs in the transition zone, but this also caused a high rate of pressure drop. Increasing the rotation angle between pitches from 60° to 80° increased the heat transfer, which increased the number of the multi-longitudinal vortices from four to eight and better mixed the cold fluid with the hot fluid near the tube wall on more paths. The friction factor decreased and the average Nusselt number increased as the Reynolds number increased. Both parameters increased as the angle of the pitch rotation increased. The performance evaluation criteria for all AEA tubes at a constant pumping power showed that the highest value (1.09) was achieved at a low Reynolds number (Re = 10,000) in the AEA 90° tube.

Keywords Turbulent flow · Heat transfer · Multi-longitudinal vortex · Field synergy principle · Performance evaluation criterion · Alternating elliptical axis tube

Nomenclature

A	Area, m^2
A	Major axes length of elliptical cross section, mm
B	Minor axes length of elliptical cross section, mm
C	Transition length, mm
C_p	Specific heat, J/(kg K)
C	Perimeter of the ellipse, m
D_h	Hydraulic diameter, m
d	Circular tube diameter of AEA tube, mm
f	Friction factor, $f = (\Delta p D_h) \Big/ \left(\frac{1}{2}\rho u_{avg}^2 L\right)$
G_k	Production of turbulence kinetic energy, kg/(m s^3)
g	Gravitational acceleration, m/s^2
h_{loss}	Irreversible head loss, m
K	Thermal conductivity, W/(m K)
k	Turbulence kinetic energy, m^2/s^2
L	Length of tube, mm
L_d	Length of inlet and outlet circular tube, mm
Nu	Nusselt number, $Nu = (q'' D_h)/(K(T_w - T_b))$
P	Pressure, kg/(m s^2)
P	Pitch length, mm
$\overline{P}$	Mean pressure, kg/(m s^2)
P_k	Improved production of turbulence kinetic energy, kg/(m s^3)
Pr	Prandtl number, $Pr = \mu C_p/K$
q''	Heat flux, W/m^2
Re	Reynolds number, Re = $\rho u D_h/\mu$
S	Strain tensor magnitude, s^{-1}
S_{ij}	Components of the mean strain tensor, s^{-1}
T	Temperature, K
T_b	Average bulk temperature, K
$\overline{T}$	Mean temperature, K
T'	Turbulent temperature fluctuations, K
u_i	Velocity, m/s
$\overline{u_i}$	Mean velocity, m/s

Technical Editor: Jader Barbosa Jr.

✉ Hamid Reza Nazif
nazif@eng.ikiu.ac.ir

[1] Department of Mechanical Engineering, Imam Khomeini International University, Imam Khomeini International University Ave., Qazvin 3414896818, Iran

u_i' Turbulent velocity fluctuations, m/s
u^* Friction velocity, m/s
V Velocity, m/s
x_i Cartesian coordinates, m
Y Distance of the closest computational node from the wall, m
y^+ Dimensionless wall distance
z Axial distance from inlet, m

Greek symbols

α Kinetic energy correction factors
δ_{ij} Kronecker delta
ε Turbulent dissipation rate, m^2/s^3
ε_{imn} Tensor of Levi–Civita
θ Angle between major axes of elliptical cross-sectional tubes
μ Laminar dynamic viscosity, kg/(m s)
μ_t Turbulent dynamic viscosity, kg/(m s)
μ_{eff} Effective dynamic viscosity, kg/(m s)
ν Kinematic viscosity, m^2/s
ρ Density, kg/m^3
σ_k Turbulent Prandtl number of k
σ_ε Turbulent Prandtl number of ε
τ_{ij} Stress tensor, kg/(m s^2)
τ_w Wall shear stress, kg/(m s^2)
Ω Characteristic rotation rate, s^{-1}
Ω_{ij} Components of the vorticity tensor, s^{-1}
Ω_m^{rot} Components of the system rotation vector, s^{-1}
ω Turbulence eddy frequency, s^{-1}

Subscripts

a Section A
avg Average
b Section B
eff Effective
s Smooth tube
w Wall

1 Introduction

Improving the thermal–hydraulic performance of heat exchangers has been a topic of interest to many engineers. Increasing heat transfer is possible by techniques such as changing the geometry of the pipe [1], using nanofluids [2–4] and applying external electromagnetic energy [5–7]. The use of fins on the tube [8–10], rotation of the cross-sectional area of the pipe [11, 12] and flattening it [13, 14] are methods of increasing heat transfer by changing the geometry of the tube.

Guo et al. [15] suggested three novel approaches of enhancing convective heat transfer of parabolic flow. One is to increase the angle between the dimensionless velocity and temperature gradient vectors (for example, using a swirl flow device) and which is now known as the field synergy principle. Li et al. [16] applied this principle to analyze numerical flow and heat transfer in alternating elliptical axis (AEA) tubes. Their experimental results indicated that the transition from laminar to turbulent flow in an AEA tube occurs at a lower Reynolds number of about 1000. Their numerical results detected the complex multi-longitudinal vortex structure of the flow. It shows improved synergy between the velocity field and temperature gradient to a large extent. They also found that AEA tubes were more appropriate than circular tubes for enhancing heat transfer at a common pumping power.

Meng et al. [17] suggested an experimental investigation on convection in an AEA tube. They analyzed heat transfer and pressure drop for a Reynolds number (Re) range of $500 < Re < 5 \times 10^4$. They found that heat transfer is more effectively enhanced with a smaller increment in flow resistance compared to other options. Their analysis showed that the mechanism for heat transfer enhancement stems primarily from the effect of multi-longitudinal vortices induced by cross-sectional changes in the AEA tubes.

Chen and Dung [18] carried out a numerical study on heat transfer characteristics in a parallel flow arrangement and counter flow in double-tube heat exchangers with AEA tubes as the inner tubes. Their numerical results showed that the inner AEA tube produced multi-longitudinal vortices in both the inner and outer tube flows and that heat transfer improved. Unlike the heat transfer coefficient of the counter flow arrangement that is often higher than the parallel flow arrangement, they observed that the performance of the parallel flow arrangement was slightly better than that of the counter flow.

Sajadi et al. [19] experimentally and numerically investigated heat transfer and flow resistance of oil flow in flattened, circular and AEA tubes. Their numerical results showed that a decrease in the aspect ratio and pitch length increased heat transfer and flow resistance. They found that AEA tubes performed better than flattened or circular tubes.

Yang et al. [11] investigated the heat transfer and flow resistance characteristics of water flow inside twisted elliptical (TE) tubes with different structural parameters in a series of experimental tests. Their results showed that TE tubes can increase heat transfer and the pressure drop inside the tube. They concluded that larger tube aspect ratios and smaller twist pitches increased the heat transfer coefficients and friction factors. They also found that the best operating regime for TE tubes was at lower Reynolds numbers. They realized that the multi-longitudinal vortex induced by the twisted tube wall improved the synergy between the velocity vector and temperature gradient, which in turn yielded better heat transfer performance.

As mentioned, AEA tubes increased the heat transfer coefficient. In this study, the turbulent flow and heat transfer in AEA tubes at different alternative angles were investigated numerically. First, the effect of the two approaches of spatial discretization of the gradients of the solution variables and sensitizing the streamline curvature to the numerical results were compared. The AEA tubes were then compared at different alternative angles for the parameters of flow, such as static pressure, velocity, wall shear stress and turbulent intensity. Comparison was made of the overall thermal–hydraulic performance of the enhanced tube, friction factor, average Nusselt number, performance evaluation criterion (PEC) and field synergy principle at a common pump power.

2 Tube geometry and mathematical model

2.1 Physical model

A series of alternate pitches with 40°, 60°, 80° and 90° rotations between the major axes of the elliptical cross-sectional tube was connected by transition sections. It generated the AEA tubes shown in Fig. 1. Note that the input and output of all AEA tubes were circular with a diameter $d = 16.5$ mm and length L_d of 34 mm. This makes the input flow condition identical at a common Reynolds number due to input into the circular cross-sectional tube. In this figure, the values of A, B, C and P are 20, 13, 6 and 34 mm, respectively, and θ is the angle between the major axes of elliptical tube cross sections.

2.2 Governing equation

The numerical simulation of turbulent flow and heat transfer was carried out using the finite volume method. The following assumptions were considered:

1) Steady-state turbulent flow.
2) The fluid is incompressible and Newtonian.
3) Viscous dissipation terms are used in the energy equation.
4) Standard eddy-viscosity models do not sensitize the effects of streamline curvature and system rotation

Based on the above assumptions, the Reynolds-averaged Navier–Stokes (RANS) equations were employed. The continuity, momentum and energy equations of the turbulent flow are [20]:

Continuity:

$$\frac{\partial \overline{u_i}}{\partial x_i} = 0. \tag{1}$$

Momentum:

$$\rho \overline{u_j} \frac{\partial \overline{u_i}}{\partial x_j} = -\frac{\partial \overline{P}}{\partial x_i} + \frac{\partial}{\partial x_j}\left(\mu \frac{\partial \overline{u_i}}{\partial x_j} - \rho \overline{u_i' u_j'}\right). \tag{2}$$

Energy:

$$\rho C_p \overline{u_i} \frac{\partial \overline{T}}{\partial x_i} = \frac{\partial}{\partial x_j}\left(K \frac{\partial \overline{T}}{\partial x_j} - \rho C_p \overline{u_i' T'} + \overline{u_i}\left(\tau_{ij}\right)_{\text{eff}}\right). \tag{3}$$

The third term on the right-hand side of the energy equation represents viscous dissipation as:

$$\left(\tau_{ij}\right)_{\text{eff}} = \mu_{\text{eff}}\left(\frac{\partial \overline{u_j}}{\partial x_i} + \frac{\partial \overline{u_i}}{\partial x_j}\right) - \frac{2}{3}\mu_{\text{eff}} \frac{\partial \overline{u_k}}{\partial x_k}\delta_{ij}. \tag{4}$$

Selection of a suitable turbulence model is crucial to modeling turbulent flow to assure the accuracy of the numerical results. Commonly used turbulence models such as standard k–ε, realizable k–ε, SST k-ω and the V2F models were used to simulate the AEA tubes. The numerical results of the friction factor and average Nusselt number of the AEA 90° tube were compared with the experimental results of Guo [21] using these models as shown in Fig. 2. It is evident that the friction factor and average Nusselt number calculated by the k–ε turbulence models were much closer to the experimental results than the other models. Considering these results and those of

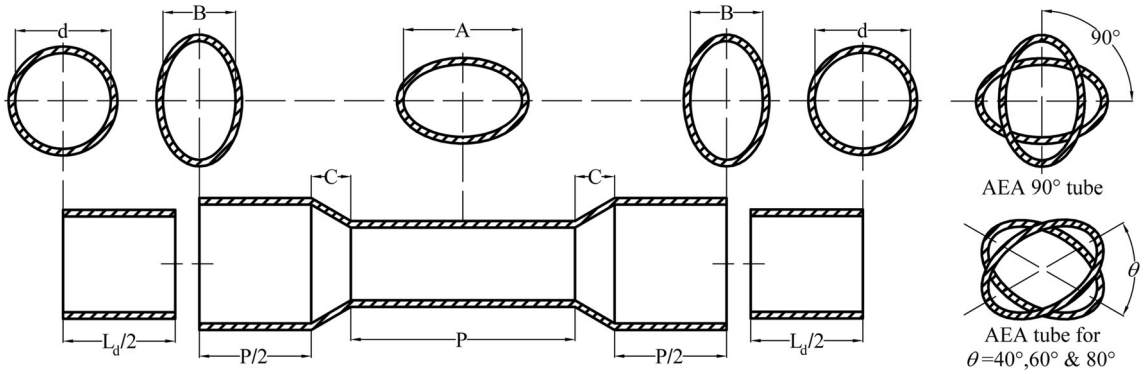

Fig. 1 Alternating elliptical axis tubes with different alternative angles

previous studies [16, 17, 22, 23], the standard k–ε turbulence model was employed for numerical simulation of turbulent flow and heat transfer of AEA tubes. The friction factor and average Nusselt number can be written as:

$$f = \frac{\Delta p D_h}{\frac{1}{2}\rho u_{avg}^2 L}, \tag{5}$$

$$Nu_{avg} = \frac{1}{L}\int_0^L \frac{q'' D_h}{K(T_w(z) - T_b(z))} dz, \tag{6}$$

where Δp is the pressure drop along the tube and $T_b(z)$ is the average bulk temperature.

$$T_b(z) = \frac{1}{A u_{avg}} \int_A uT dA. \tag{7}$$

The turbulence kinetic energy (k) and its dissipation rate (ε) equations were obtained from the following transport equations [24]:

$$\frac{\partial}{\partial x_i}(\rho k \overline{u_i}) = \frac{\partial}{\partial x_j}\left[\left(\mu + \frac{\mu_t}{\sigma_k}\right)\frac{\partial k}{\partial x_j}\right] + P_k - \rho\varepsilon, \tag{8}$$

$$\frac{\partial}{\partial x_i}(\rho \varepsilon \overline{u_i}) = \frac{\partial}{\partial x_j}\left[\left(\mu + \frac{\mu_t}{\sigma_\varepsilon}\right)\frac{\partial \varepsilon}{\partial x_j}\right] + C_{1\varepsilon}\frac{\varepsilon}{k}P_k - \rho C_{2\varepsilon}\frac{\varepsilon^2}{k}, \tag{9}$$

where μ_t is the turbulent dynamic viscosity and P_k is the improved production of turbulence kinetic energy (Eq. 16) due to the mean velocity gradients (see Sect. 4.4).

$$\mu_t = \rho C_\mu \frac{k^2}{\varepsilon}. \tag{10}$$

The standard k–ε turbulence model constants are [24]: $C_{1\varepsilon} = 1.44$, $C_{2\varepsilon} = 1.92$, $C_\mu = 0.09$, $\sigma_k = 1$ and $\sigma_\varepsilon = 1.3$.

2.3 Boundary conditions

The inlet velocity of the AEA tube was determined by calculating the Reynolds number of the flow at the tube inlet assuming that it is uniform and normal to the boundary. In Guo's experiment [21], the difference between the maximum and minimum temperature was less than 30°; therefore, the inlet and wall temperature were equal to 295 and 325 K, respectively. Along the tube wall, the no-slip boundary condition for velocity was imposed.

3 Numerical method

The SIMPLEC algorithm [25] was employed to handle the pressure–velocity coupling for all numerical simulations. The pressure-based coupled algorithm [26] was used to solve the governing equations. For a coupled system of turbulent flow and energy, the gradients of the solution variables of the grids were set by least squares cell-based (LSCB) [27] and green Gauss node-based (GGNB) [28, 29] approaches, respectively. First, the flow and turbulence equations were solved and then the flow and turbulent variables were frozen and the energy equation solved. The standard [27] and second-order upwind [30] schemes were adopted to calculate the cell face pressure and discretize all equations, respectively. The enhanced wall treatment [31] method was used to handle the near-wall phenomena of the tube wall. The double precision solver was used and numerical calculation was stopped when the resulting residuals for all equations were lower than 10^{-6}.

4 Numerical computation

4.1 Grid independence

To test the independence of the generated grids, five grids of different sizes were tested for each AEA and round tube. Figure 3 shows the cross-sectional grid layout used in the present numerical computation for the AEA 90° and 60° tubes and the round tube. The average Nusselt numbers (Nu_{avg}) of the five computational grids are listed in Table 1

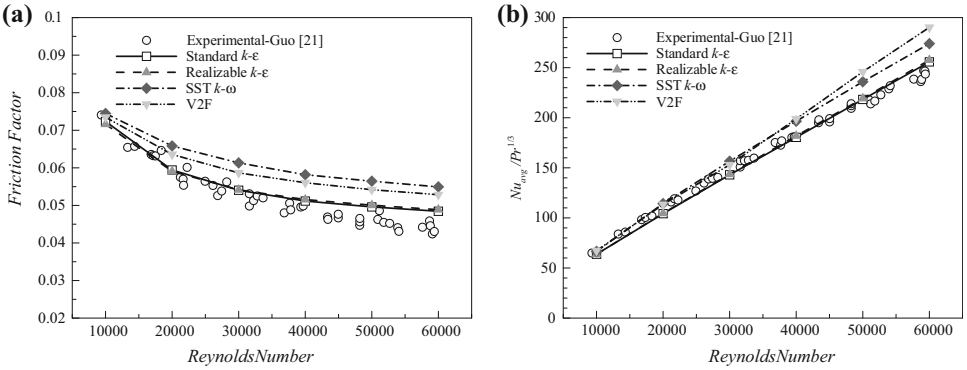

Fig. 2 Validation of turbulence models by comparison of numerical results with experimental results of Guo [21] in the AEA 90° tube: **a** friction factor; **b** average Nusselt number

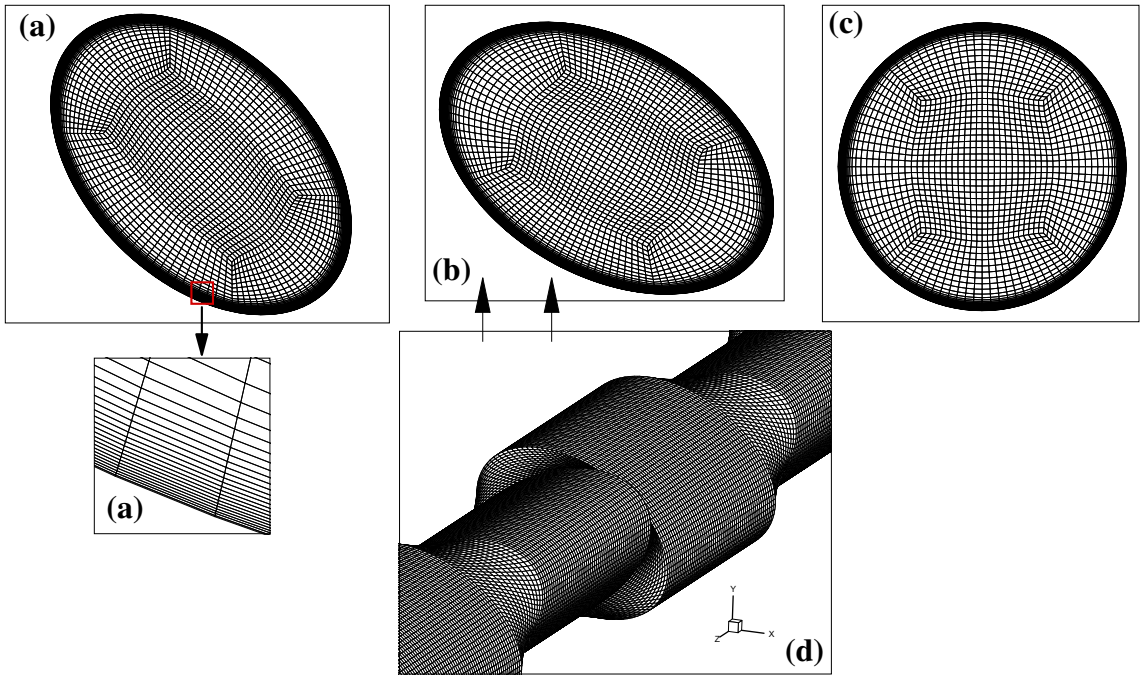

Fig. 3 Cross-sectional grid of the AEA tube: **a** 90°; **b** 60°; **c** circular tube; **d** 3D view of the AEA 60° tube

Table 1 Results of grid independence study for the AEA 90° tube

Mesh (number of cells)	Nu_{avg}	δNu_{avg}
Mesh-1 (1,444,608)	280.9442	–
Mesh-2 (1,932,800)	339.2751	− 58.3309
Mesh-3 (3,379,376)	343.5931	− 4.318
Mesh-4 (3,951,360)	345.0233	− 1.4302
Mesh-5 (4,646,340)	346.0065	− 0.9832

for the AEA 90° tube under turbulent flow at $Re = 40{,}000$. The increasing grid numbers along the x, y and z axes below the third row of Table 1 indicate that the relative deviation of the average Nusselt number did not change significantly. The mesh-4 grid (3,951,360 cells) for the AEA 90° tube was selected for all numerical simulations of the AEA tubes.

Because the enhanced wall treatment method was used to simulate the boundary layer motion, the distance of the tube walls to the nodes of all grids is the value of the dimensionless wall distance parameter called y^+ which is close to or less than one. The y^+ parameter is defined as [20]:

$$y^+ = \frac{u^* Y}{v}, \tag{11}$$

where Y is the distance of the first node from the wall of the tube, v is the kinematic viscosity of the fluid and u^* is the friction velocity as defined by [20]:

$$u^* = \sqrt{\frac{\tau_w}{\rho}}. \tag{12}$$

Based on the above equations, the distance of the nearest node to the tube wall is 0.005 mm and the value of y^+ is approximately one. Figure 4 shows the y^+ parameter along the AEA 90° tube at $Re = 60{,}000$. It shows that all y^+ parameters were close to or less than one.

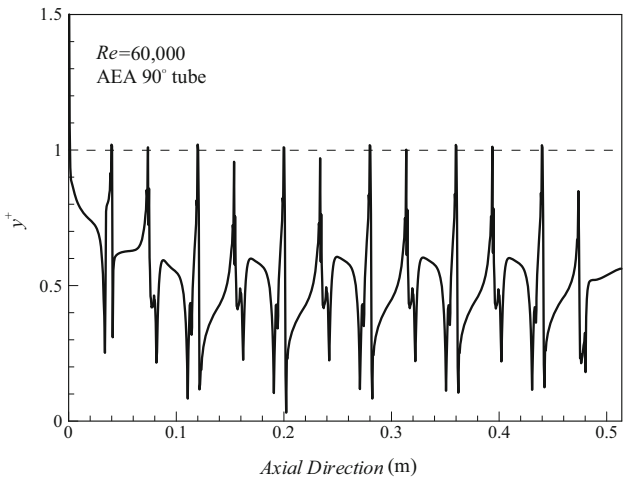

Fig. 4 Local values of non-dimensional y^+ parameter along the AEA 90° tube at $Re = 60{,}000$

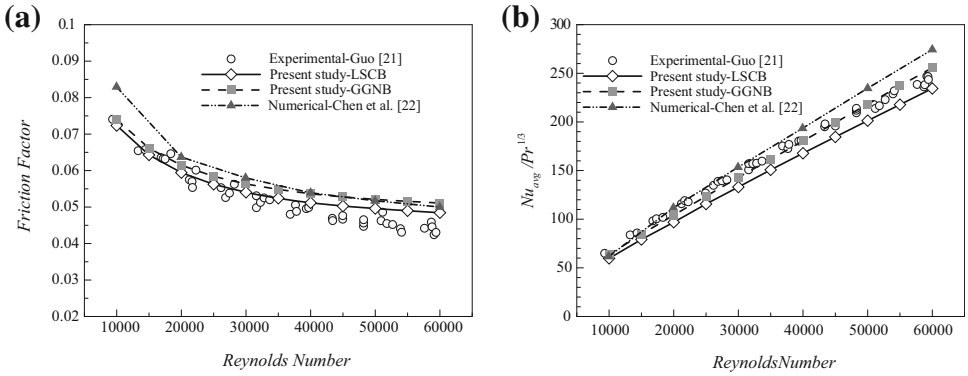

Fig. 5 Comparison of the numerical results with experimental [21] and numerical [22] results for the AEA 90° tube: **a** friction factor and **b** average Nusselt number

4.2 Validation of the numerical simulation for the AEA tube

To ensure the accuracy of the numerical computations, the simulation results were compared with experimental data. Guo [21] analyzed the increase in heat transfer for the turbulent flow in the AEA 90° tube and the parameters of this study were used. Figure 5 compares the numerical friction factor and average Nusselt number for an AEA 90° tube from the present study and from the experimental study of Guo [21] and a numerical study by Chen et al. [22]. Figure 5 shows that the numerical results are in good agreement with the experimental results reported by Guo [21]. The figures also show that the numerical results from the present study are better than the numerical data by Chen et al. [22].

The maximum absolute error observed between the numerical and experimental results for friction factor and average Nusselt number of an AEA 90° tube were about 14 and 6.5%, respectively. The maximum absolute errors for these kinds of tubes were less than those reported by Sajadi et al. [19] (21 and 24% for friction factor and Nusselt number, respectively). It can be concluded that the numerical computational model was appropriate for solving convective heat transfer of the turbulent flow problem in the AEA tubes.

As shown in Fig. 5a, the friction factor using the computational LSCB approach for the gradients of the solution variables is closer to the experimental results than that from the GGNB approach. The average Nusselt number calculated using the GGNB was the best for the energy equation according to the results presented in Fig. 5b. According to this, the LSCB and GGNB approaches are appropriate for turbulent flow and the energy equation, respectively.

4.3 Validation of numerical simulation for a circular tube

The circular tube was simulated to compare the numerical results of the AEA tube with those of the circular tube under the same conditions. In a fully developed flow, the friction factor correlation for the circular smooth surface tubes at $3000 \lesssim Re \lesssim 5 \times 10^6$ was determined by Petukhov et al. [32]. The experimental correlation for the Nusselt number in the fully developed flow valid for circular tubes was determined by Gnielinski [33, 34]. These correlations are valid for $3000 \lesssim Re \lesssim 5 \times 10^6$ and $0.5 \lesssim Pr \lesssim 2000$ and were calculated as follows:

$$f_s = (0.79\ln(Re) - 1.64)^{-2}, \tag{13}$$

$$Nu_s = \frac{(f/8)(Re - 1000)Pr}{1 + 12.7(f/8)^{1/2}(Pr^{2/3} - 1)}. \tag{14}$$

Figure 6 compares the numerical results for the friction factor and average Nusselt number for the circular tube in the present study for fully developed flow using the above correlations. Good agreement exists between the present numerical results and the experimental correlations.

4.4 The effect of sensitizing streamline curvature and system rotation on numerical results

One drawback of eddy-viscosity models in two-equation models is insensitivity to streamline curvature and system rotation, which play significant roles in many turbulent flows of practical interest [35]. In the current study, the effect of streamline curvature and system rotation on the simulation results of the AEA 90° tube was investigated. An empirical function [36] can be applied to account for the streamline curvature and system rotation effects as follows:

$$f_{\text{rotation}} = (1 + C_{r1})\frac{2r^*}{1 + r^*}\left[1 - C_{r3}\tan^{-1}(C_{r2}\tilde{r})\right] - C_{r1}. \tag{15}$$

To improve the production term, the multiplier used was limited as follows:

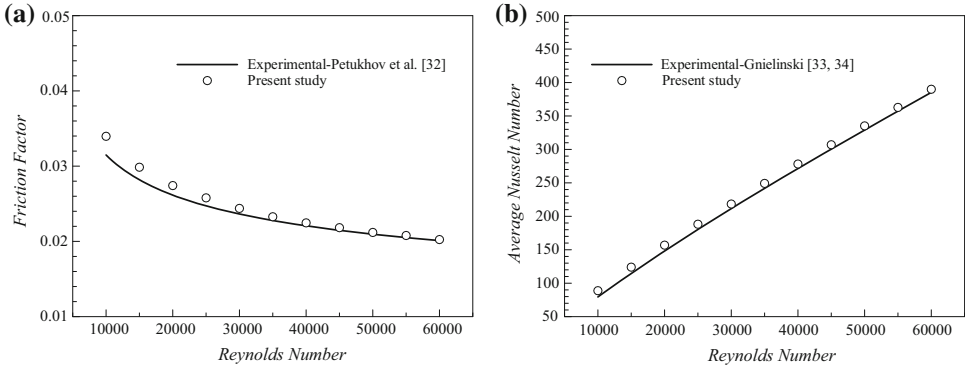

Fig. 6 Comparison of the numerical results with experimental correlations of Petukhov et al. [32] and Gnielinski [33, 34], respectively, for a circular tube: **a** friction factor and **b** average Nusselt number

Table 2 Comparison of numerical simulation with and without sensitizing streamline curvature and system rotation

Re	Curvature correction	*f*	Number of iterations	Difference %
30,000	Without	0.05414584	1296	0.199
	With	0.05403832	1418	
60,000	Without	0.04850669	1550	0.132
	With	0.04844259	1759	

$$P_{\mathrm{k}} = G_{\mathrm{k}} \cdot f_r, \tag{16}$$

where

$$G_{\mathrm{k}} = -\rho\overline{u_i' u_j'}\frac{\partial \overline{u_j}}{\partial x_i}, \tag{17}$$

$$f_r = \max\left\{0.1 + C_{\mathrm{scale}}\left(\tilde{f}_r - 1\right)\right\}, \tag{18}$$

$$\tilde{f}_r = \max\{\min(f_{\mathrm{rotation}}, 1.25).0\}. \tag{19}$$

The empirical constants C_{r1}, C_{r2}, C_{r3} and C_{scale} were equal to 1, 2, 3 and 1, respectively. The r^* and $\tilde{r}$, terms of the f_{rotation} function, can be expressed as follows [35, 37]:

$$r^* = \frac{S}{\Omega}, \tag{20}$$

$$\tilde{r} = 2\Omega_{ik}S_{jk}\left[\overline{u_t}\frac{\partial S_{ij}}{\partial x_t} + \left(\varepsilon_{imn}S_{jn} + \varepsilon_{jmn}S_{in}\right)\Omega_m^{\mathrm{rot}}\right]\frac{1}{\Omega D^3}, \tag{21}$$

where the first term in brackets is the second velocity gradient and the second term in brackets is a measure of system rotation. Furthermore, ε_{imn} is the Levi–Civita tensor. The strain rate and vorticity tensor [37] are:

$$S_{ij} = \frac{1}{2}\left(\frac{\partial \overline{u_i}}{\partial x_j} + \frac{\partial \overline{u_j}}{\partial x_i}\right), \tag{22}$$

$$\Omega_{ij} = \frac{1}{2}\left(\frac{\partial \overline{u_i}}{\partial x_j} - \frac{\partial \overline{u_j}}{\partial x_i}\right) + 2\varepsilon_{mji}\Omega_m^{\mathrm{rot}}, \tag{23}$$

where

$$S^2 = 2S_{ij}S_{ij}, \tag{24}$$

$$\Omega^2 = 2\Omega_{ij}\Omega_{ij}, \tag{25}$$

$$D^2 = \max\left(S^2, 0.09\omega^2\right), \tag{26}$$

in which S_{ij} is the component of the mean strain tensor, Ω_{ij} the component of the vorticity tensor, Ω_m^{rot} the component of the system rotation vector, S the strain tensor, Ω the vorticity tensor and ω the turbulence eddy frequency.

The numerical results of the friction factor from Eq. (16) at $Re = 30{,}000$ and 60,000 are presented in Table 2. This table shows that the sensitizing effects of streamline curvature and system rotation did not play an important role in the flow and turbulence simulation for this type of tube. The results show that the friction factor improved by less than 0.2%. The number of iterations for convergence increased without an appreciable difference in the final results. Therefore, the sensitizing effects of streamline curvature and system rotation for this study were negligible.

5 Results and discussion

The thermal–hydraulic performance of turbulent flow of a fluid and the heat transfer in an AEA tube were simulated numerically. Variables such as pressure drop, velocity magnitude, wall shear stress, turbulent intensity, friction factor, average Nusselt number, PEC and field synergy principle were determined.

Figure 7 shows the part of the AEA tube at 0.357–0.437 m in length. As seen in this figure, two sections are denoted as Distances A and B. Between them is a

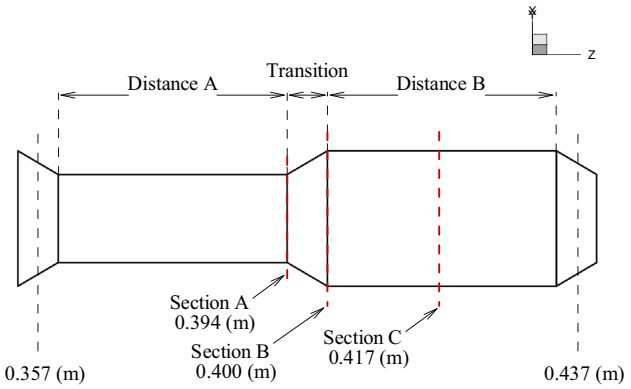

Fig. 7 Positions of the three sections

distance denoted as the transition length and is shown in the figure as "transition". In the area shown in Fig. 7, three sections were selected as perpendicular to the flow for which the numerical results are displayed. Sections A and B are positioned at the input and output of the transition zone, respectively, and the midpoint of Distance B is denoted as Section C.

Note that the cross-sectional area of the middle of the transition zone in the AEA tubes are different. Figure 8 shows that the shape of this cross section at angle θ values of 40°, 60° and 80° varied from ellipsoid to square. Figure 9 shows the distribution of the area along an alternating cycle of the tube, especially in the transition zone. The figure shows that increasing angle θ from 40° to 80° decreased the area at the middle of the transition zone, but that this increased at the 90° angle. This increase in the middle of the transition zone from the AEA 80° to the 90° tubes caused a considerable difference in the results of the numerical solution (see Sect. 5.1). The largest area was observed in the transition zone of the AEA 90° tube that, as shown in Fig. 8, was circular in shape. Note that the minimum cross-sectional area was observed at the middle of the transition zone of the AEA tube for angles less than 80°, but the maximum was observed for AEA 90° tube. Also, the transition zones were created with a constant perimeter of cross sections.

5.1 Pressure drop results

When designing efficient heat exchangers, the pressure drop throughout the tube length is important. Figure 10 shows the average static pressure along Distance A, the transition zone and Distance B of the AEA tube at different values of θ. Figure 10 shows the maximum rate of pressure drop, which occurred at the transition zone.

Figure 11 shows the average velocity in a complete alternating cycle of the AEA tube. Figures 9 and 11 show that emergence of the maximum area in the cross section at the middle of the transition zone of the AEA 90° tube decreased the average velocity in that zone. This conforms with the law of mass conservation ($A_aV_a = A_bV_b$). The other tubes considered in this study experienced a decrease in this part of the cross-sectional area, which increased the average velocity in that zone.

The average velocity exiting the transition zone increased compared to the entry of the flow of that zone for all tubes. For all AEA tubes except the 90°, the decrease in the cross-sectional area at the middle of the transition zone showed displacement acceleration in that area. This caused an increase in the average velocity at the outlet section of the transition zone toward the inlet section. For the AEA 90° tube, the fluid flow experienced a lower pressure drop after crossing from Section A because of the increase in the cross-sectional area in the middle of the transition zone. Away from the middle of the transition zone, the decrease in the area of the outlet section increased the velocity at the outlet section of the transition zone compared to the inlet section.

This difference in velocity in the inlet and outlet sections of the transition zone influenced the average static pressure of the tube cross sections. An energy equation was developed by assuming steady and incompressible one-dimensional flow and showed that considerable local head loss (h_{loss}) of pressure was observed in the transition zone. The energy equation was as follows:

$$P_b = P_a - \rho\left(\alpha_b V_b^2 - \alpha_a V_a^2\right)/2 - \rho g h_{\text{loss}}, \tag{27}$$

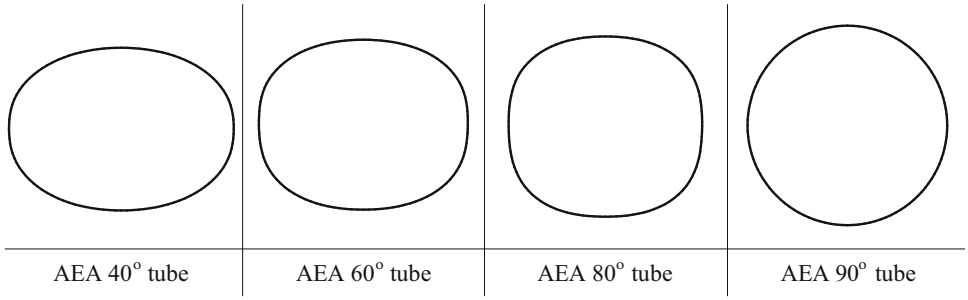

Fig. 8 Cross section of the middle of the transition zone of all AEA tubes

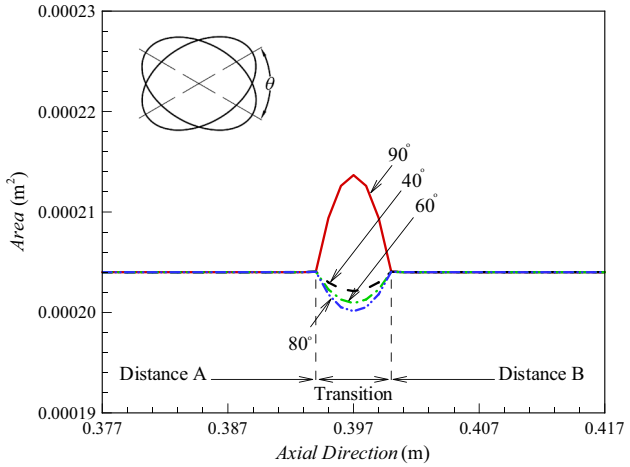

Fig. 9 Cross-sectional areas along the axial direction of the AEA tubes at different angles

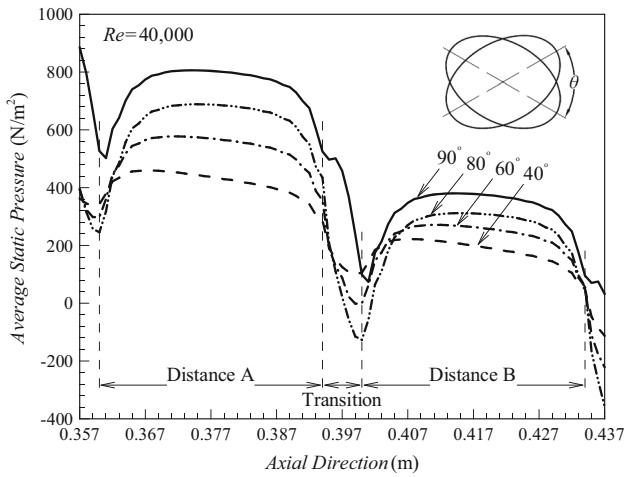

Fig. 10 Average static pressure along the axial direction of the AEA tubes at different angles

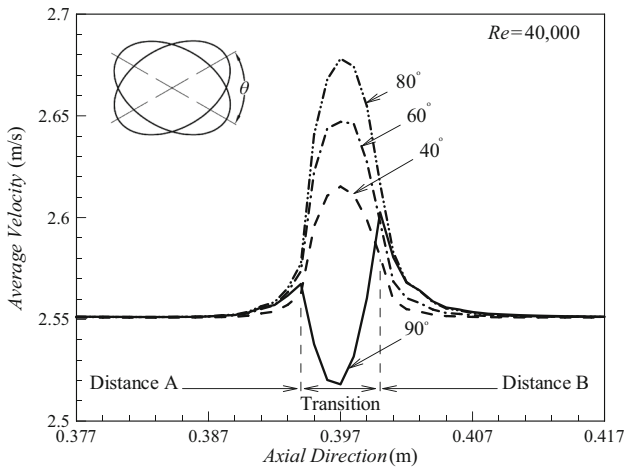

Fig. 11 Average velocity along the axial direction of the AEA tubes at different angles

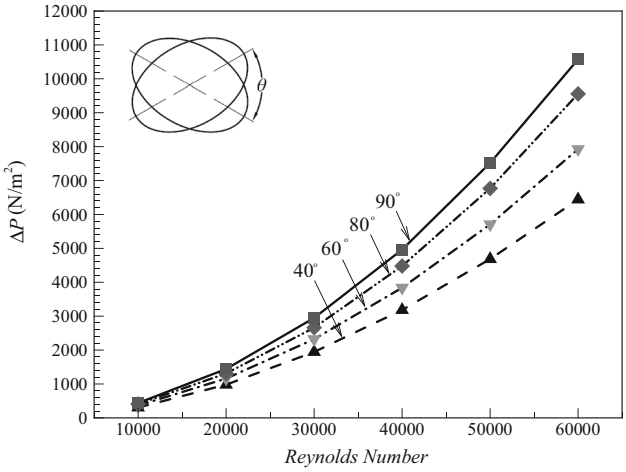

Fig. 12 Pressure drop at different Reynolds numbers of the AEA tubes at different angles

where h_{loss}, α_a and α_b are the irreversible head loss of the transition zone and the kinetic energy correction factors in Sections A and B, respectively [38].

Figure 12 shows the pressure drop for the AEA tubes at different Reynolds numbers. In AEA tubes with greater angles, the pressure drop curves were more sensitive to changes in the Reynolds number. An increase in the Reynolds number increased the pressure drop and the difference between the pressure drops in the various tubes increased as angle θ increased.

5.2 Wall shear stress results

The shear stress on the tube wall represents the force impeding the motion of the fluid at a distance from the tube inlet. It was necessary to determine in which areas of the tube the stress was critical and severe; therefore, the average wall shear stress and its effect on pressure drop were calculated. The wall shear stress was computed as the multiplication of the average effective viscosity (sum of the laminar and turbulent viscosity) by the velocity gradient as follows [20]:

$$\tau_{\text{w.avg}} = (\mu + \mu_t)_{\text{avg}} \left(\nabla V + \nabla V^T\right)_{\text{avg}}. \tag{28}$$

Note that the average effective viscosity and velocity gradient on the sections of the tube wall were computed as follows:

$$(\mu + \mu_t)_{\text{avg}} = \frac{1}{C} \int (\mu + \mu_t) \mathrm{d}C, \tag{29}$$

$$\left(\nabla V + \nabla V^T\right)_{\text{avg}} = \frac{1}{C} \int \left(\nabla V + \nabla V^T\right) \mathrm{d}C. \tag{30}$$

Figure 13a, b shows the average value of the effective viscosity and velocity gradient on the sections of the wall,

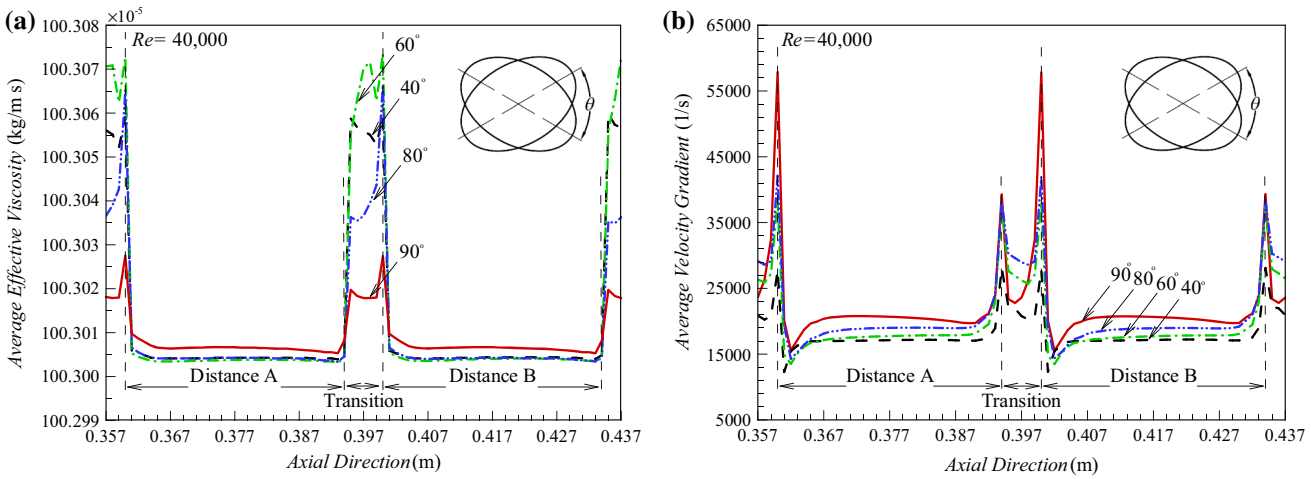

Fig. 13 **a** Average of the effective viscosity and **b** velocity gradient in the wall shear stress equation along the axial direction of the AEA tubes at different angles

respectively. Figure 13a shows that the effective viscosity in the transition zone was only sensitive to the variation in angle θ. The values for the AEA 90° tube as compared to the other tubes were a little larger along a constant cross section. Figure 13b shows that the average velocity gradient at Distances A and B increased as angle θ increased. The average velocity gradient for the AEA 90° tube in the transition zone was compared to those of other tubes and showed different results because of the different cross-sectional areas of the other tubes. Equation (28) and Fig. 13a, b indicate that the term most effecting wall shear stress was the velocity gradient term, which produced stronger changes than the viscosity term.

Figure 14 shows the average shear stress on the sections of the tube wall and indicates that an increase in angle θ increased the wall shear stress. The figure shows that the change in average wall shear stress for the AEA 90° tube differed from those of other AEA tubes in the transition zone. This occurred because of the difference in the cross-sectional area of the middle of the transition zone for the AEA 90° tube.

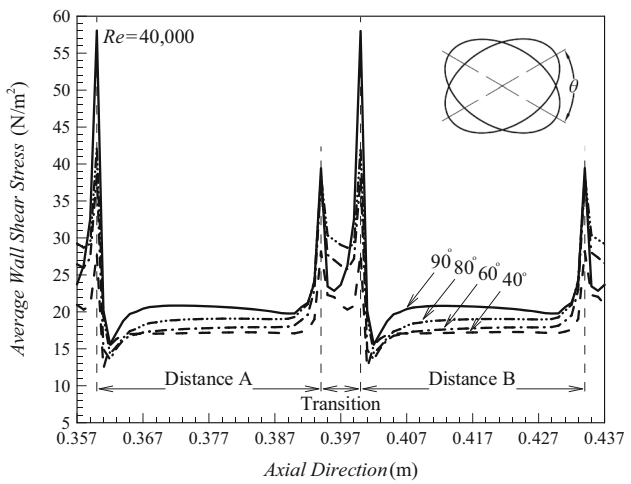

Fig. 14 Average wall shear stress along the axial direction of the AEA tubes at different angles

5.3 Flow structure

Figure 15 shows the effect of angle θ on the flow structure in the streamlines in Section C of all AEA tubes. In the AEA 40° and 60° tubes, there are four vortices in the tube cross section and an increase in angle θ from 60° to 80° divided the multi-longitudinal vortices and increased the number from four to eight. The results showed that the presence of multi-longitudinal vortices along the length of the tube increased the pressure loss of the flow.

5.4 Heat transfer results

Figure 16 shows the temperature contour and the velocity vectors in Section C of the AEA tubes used to determine the effect of angle θ on the heat transfer of turbulent flow. As seen, the cold fluid moved toward the tube wall from the center of the tube. During this impingement, the cool fluid from the center of the tube mixed with the hot fluid near the wall and the heated fluid near the wall moved toward the core flow region because of the presence of secondary flows. The number of multi-longitudinal vortices increased as angle θ increased and caused the cold fluid to better mix with the hot fluid on more paths, resulting in increased heat transfer.

The average Nusselt number along the AEA tubes at different values for angle θ are shown in Fig. 17. The value of the average Nusselt number in the transition zone was high compared with the other areas. At some distance from this area, the average Nusselt number decreased. It can also

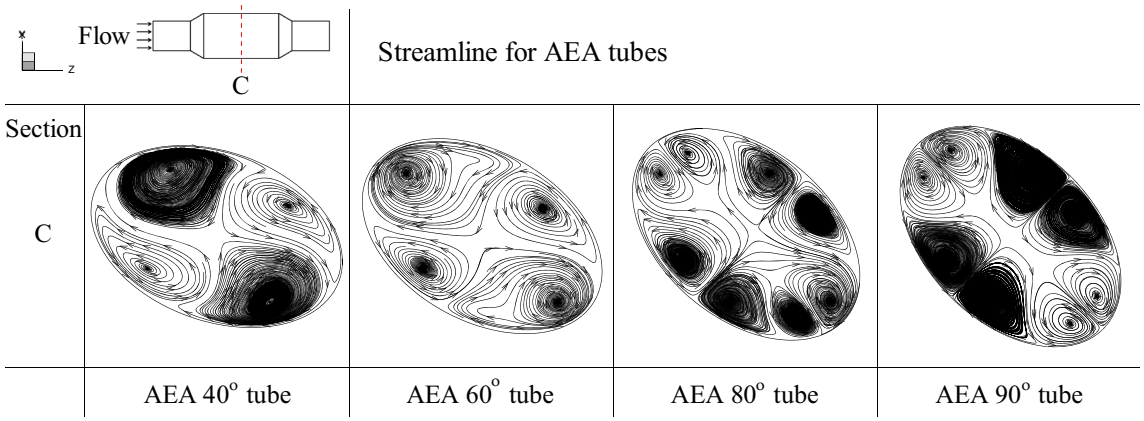

Fig. 15 Streamline on Section C of all AEA tubes at $Re = 40{,}000$ at different angles

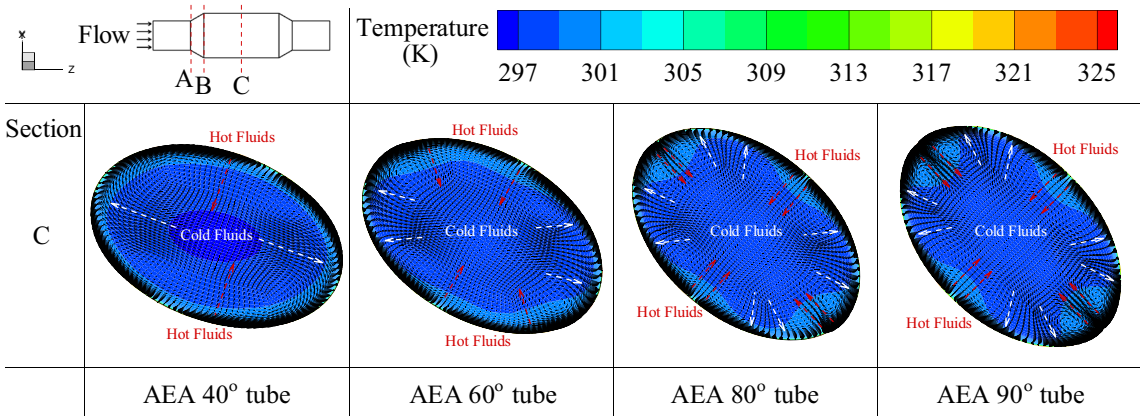

Fig. 16 Temperature contour and velocity vector on Section C of AEA tubes at $Re = 40{,}000$ and different angles

be observed that increasing angle θ increased the heat transfer value. The following equation was used to calculate the average Nusselt number:

$$Nu_{\text{avg}} = \frac{q''_{\text{avg}} D_{\text{h}}}{K(T_{\text{w}} - T_{\text{b}})}, \tag{31}$$

where $q_{\text{avg}}{}''$ is the average heat flux on the tube wall and T_{w} and T_{b} are the wall and bulk temperature of the fluid, respectively.

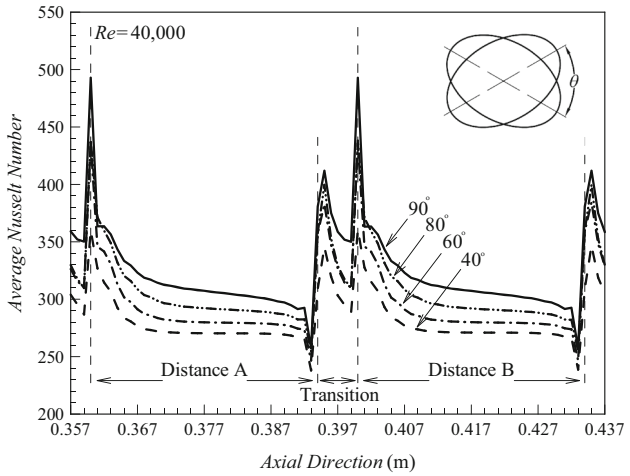

Fig. 17 Average Nusselt number along the axial direction of the AEA tubes at different angles

5.5 Turbulent intensity

Another parameter that reflects the strength of fluid mixing is turbulent intensity, which represents the heat transfer performance to some extent in the turbulent flow. Figure 18 shows the contour of the turbulent intensity in three cross sections. The turbulent intensity is higher at both ends of the main diagonal of the studied sections than in other areas. Section B shows a greater area of high turbulent intensity. The turbulent intensity in Section B is high and increased the heat exchange with the hot fluid near the wall, increasing the heat transfer. The turbulent intensity can be seen to increase with an increase in angle θ.

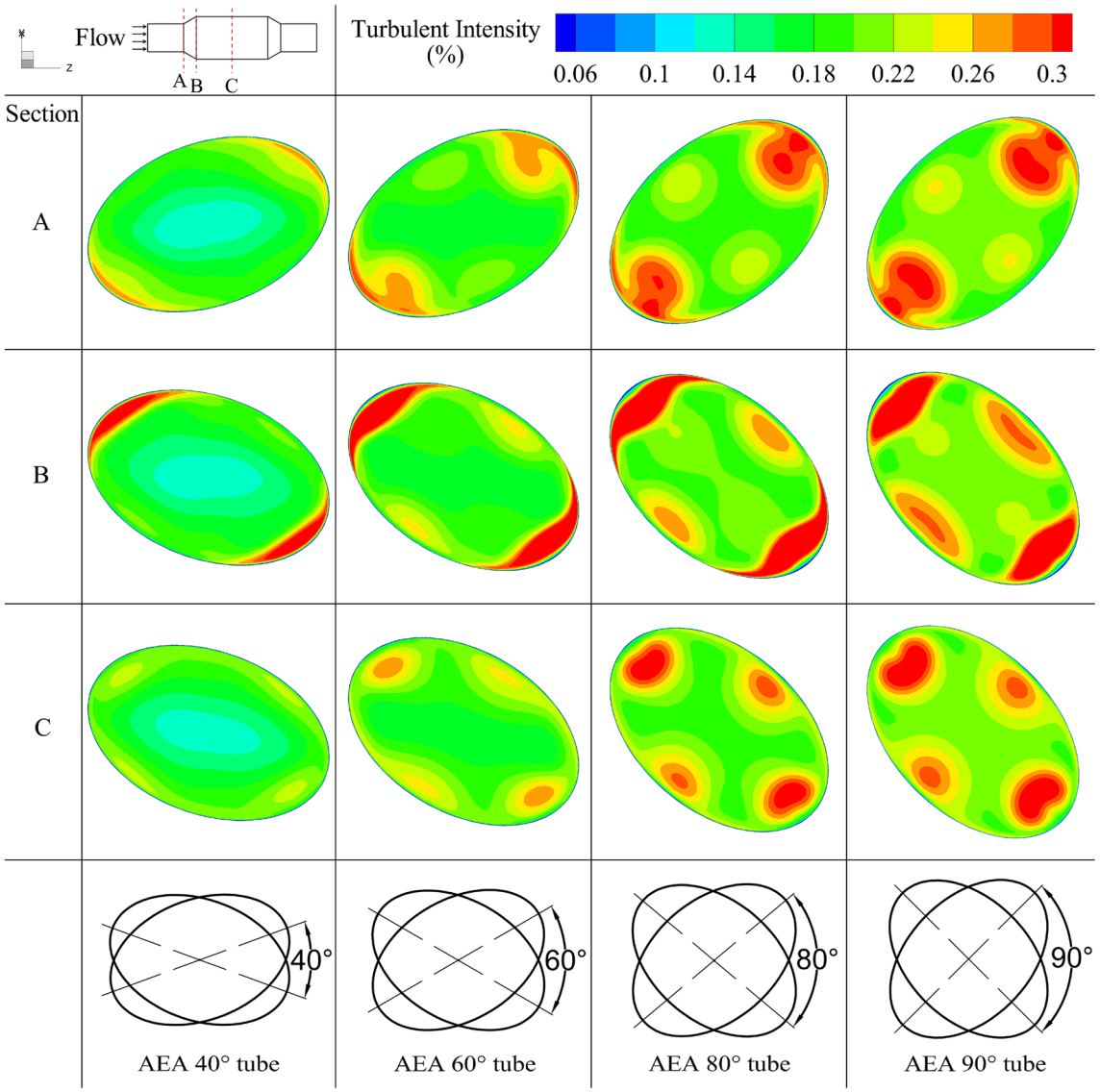

Fig. 18 The turbulent intensity contour in sections of the AEA tubes at different angles at $Re = 40{,}000$

5.6 Analysis from field synergy principle

In the field synergy principle, an improvement in synergy between the velocity vector and temperature gradient will increase the convective heat transfer. Creation of multi-longitudinal vortices in the fluid flow is one way to increase synergy between these two parameters [15]. Figure 19 shows the contours of the numerical value of the dot products of the velocity vector and temperature gradient in Sections A, B and C. It can be observed that Sections A and B have a maximum value of $V \cdot \nabla T$ and an increase in angle θ divided the zones from two into eight segments. Farther away from the transition zone, the $V \cdot \nabla T$ in Section C between the multi-longitudinal vortices and the tube wall reached a maximum value and increasing angle θ increased the maximum value of the dot product.

For more accurate analysis, the sum of the dot products of the velocity vector and temperature gradient at the left-hand side of the integral of Eq. (32) was calculated for Sections A–B, B–C and A–C (Table 3). It should be noted that Section A–B represents Sections A and B. When integrating the energy equation over the entire domain, regardless of axial heat conduction within the fluid, the amount of heat transferred from the tube wall related to the dot product of the velocity vector and temperature gradient as follows [39]:

$$\int_{\text{inlet and outlet}} \rho C_{\text{p}}(V \cdot \nabla T)\mathrm{d}A = \int_{\text{wall}} \vec{n} \cdot K_{\text{eff}} \nabla T \mathrm{d}L = q_{\text{w}}, \tag{32}$$

where $\vec{n}$ is the outward normal along each boundary and q_{w} is heat transfer at the tube wall.

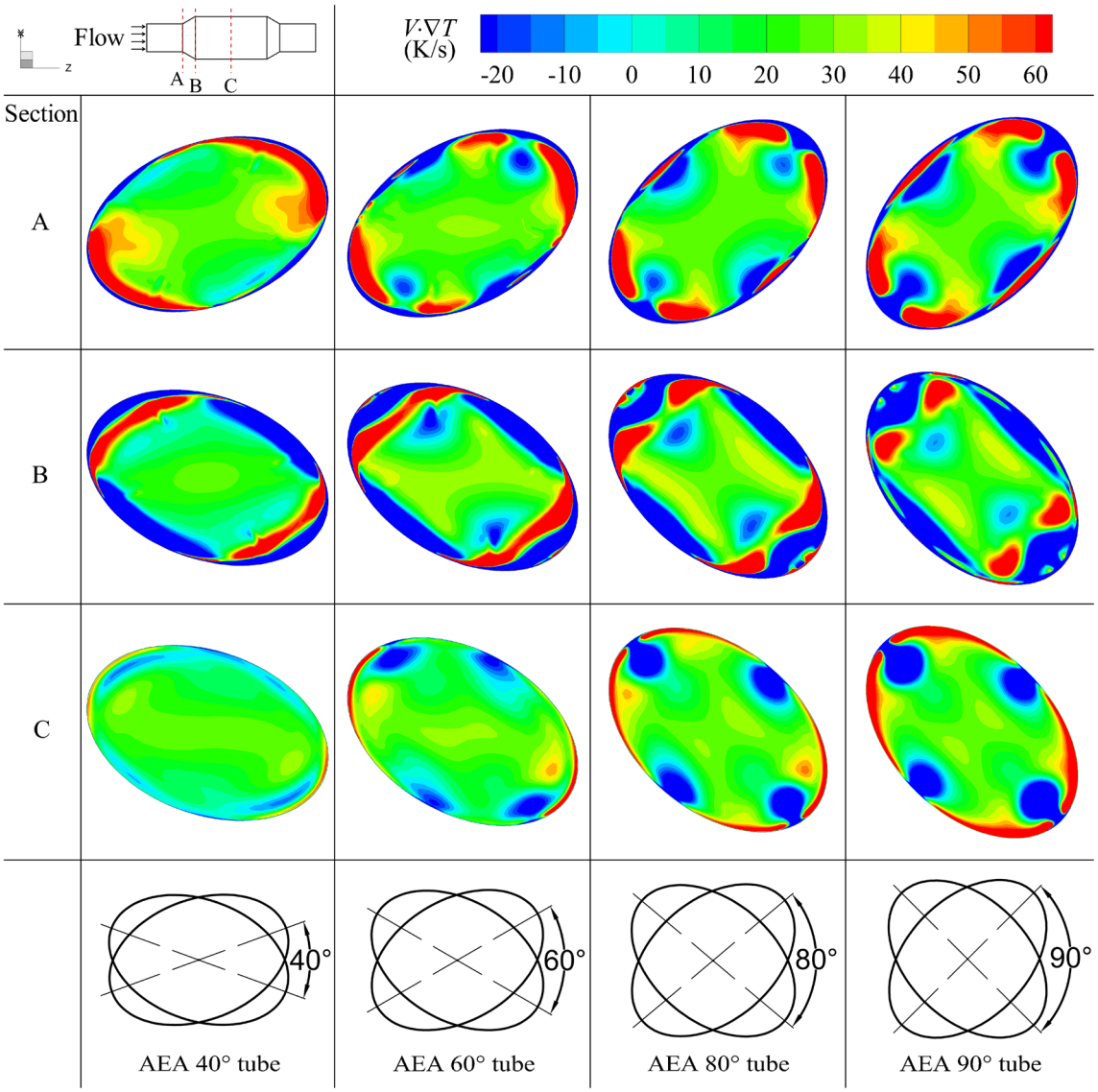

Fig. 19 Contours of $V \cdot \nabla T$ in sections of the AEA tubes at different angles at $Re = 40{,}000$

Table 3 Sum of $V \cdot \nabla T$ in sections of AEA tubes at $Re = 40{,}000$

$\int_{\text{Sec.}} (V \cdot \nabla T) \mathrm{d}A$	AEA 40° tube	AEA 60° tube	AEA 80° tube	AEA 90° tube
Sec. A and B	7.1100×10^{-03}	2.5365×10^{-02}	2.5860×10^{-02}	4.7752×10^{-02}
Sec. B and C	9.9296×10^{-04}	-1.0327×10^{-02}	-9.7976×10^{-03}	-1.6751×10^{-02}
Sec. A and C	8.1029×10^{-03}	1.5038×10^{-02}	1.6062×10^{-02}	3.1001×10^{-02}

As seen in Table 3, the sum of $V \cdot \nabla T$ in Section A–B is larger than in Section B–C. Equation (32) indicates that heat transfer in the transition zone increased. In addition, the sum of this dot product in Section B–C was negative, which indicates that the flow exchanged heat with the fluid throughout the tube because of the reverse flow after the transition zone (according to the results of Chen et al. [22]). The increase in angle θ increased the sum of the dot products of the velocity vector and temperature gradient in Section A–C, indicating that heat transfer increased. It can be concluded that the multi-longitudinal vortices have increased the angle between the velocity vector and temperature gradient, resulting in an increase in heat transfer.

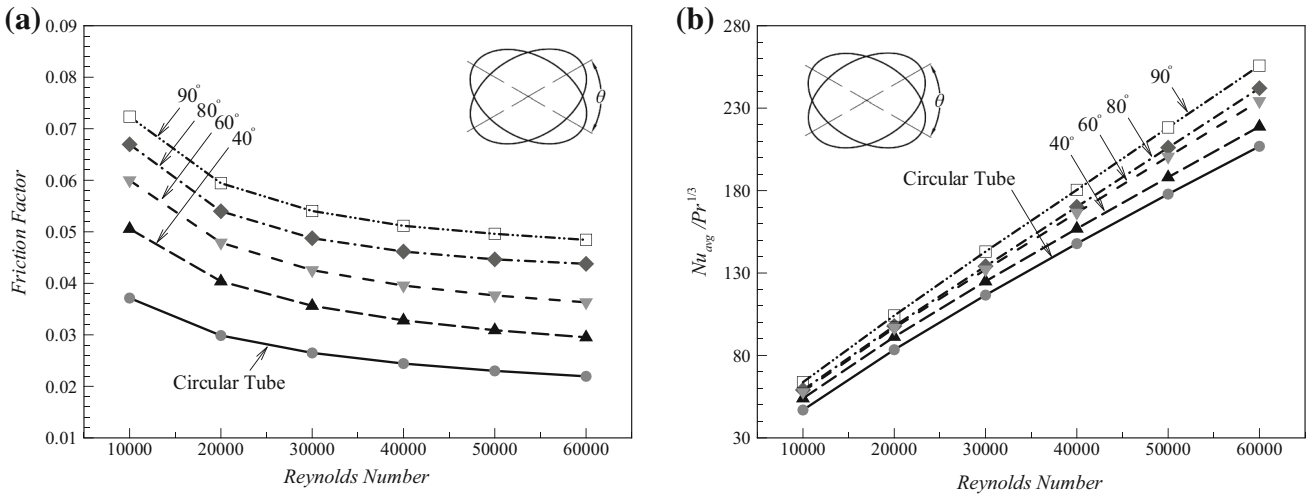

Fig. 20 **a** Friction factor and **b** average Nusselt number for increase in Reynolds number

5.7 Friction factor and average Nusselt number

The thermal–hydraulic performance of the AEA tubes and the circular tube were investigated by calculating the friction factor and average Nusselt number at $Re = 10{,}000$ to 60,000. Figure 20a, b shows that the friction factor decreased and the average Nusselt number increased as Re increased. An increase in the angle of the pitch rotation also caused both parameters to increase. It was found that the AEA 90° tube showed the highest heat transfer, but a drawback to this increase was an increase in the pressure drop.

5.8 Performance evaluation criterion

The performance evaluation criterion (PEC) was developed by Webb and Kim [40] to evaluate the overall thermal–hydraulic performance of the enhanced tube at a common pump power. The PEC is calculated as:

$$\mathrm{PEC} = \frac{Nu/Nu_{\mathrm{s}}}{(f/f_{\mathrm{s}})^{1/3}}, \tag{33}$$

where Nu_{s} and f_{s} are the Nusselt number and friction factor in a smooth tube, respectively.

The variation in PEC with an increase in Re in the AEA tubes at different values of angle θ is shown in Fig. 21. As seen, at $Re \geq 20{,}000$, the PEC for all tubes was less than one. The highest PEC value for each AEA tube was obtained at a low Reynolds number. At $Re = 10{,}000$, the PEC increased as angle θ increased (except for the AEA 80° tube). The maximum PEC of 1.09 was obtained in the AEA 90° tube for the lowest Reynolds number, which indicates that this tube is more economical than the circular tube. It is evident that increasing the number of multi-longitudinal vortex flows by increasing angle θ increased heat transfer better than at smaller values for angle θ.

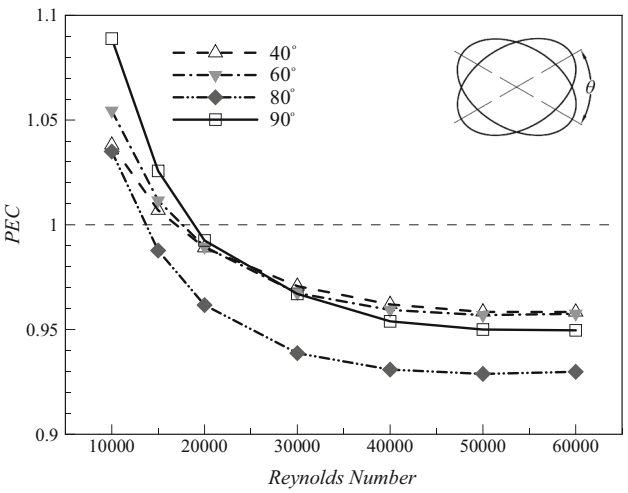

Fig. 21 Variation in PEC at different angles of the AEA tubes

6 Conclusions

In this research, the effects of multi-longitudinal vortex generation and various rotation angles between the pitches of alternating elliptical axis tubes on heat transfer and pressure drop of turbulent flow was numerically investigated. All numerical simulations were done at $Re = 10{,}000$ to 60,000. The standard k–ε turbulence model showed reasonable conformity with the experimental results in relation to the numerical results for friction factor and average Nusselt number. The LSCB and GGNB approaches were also suitable for discretizing the gradients of the solution variables of turbulent flow and the energy

equation, respectively. Adding the function of curvature correction in the turbulence model had no significant effect on the numerical solution; however, the friction factor improved to less than 0.2% by adding this function.

Observation of the pressure drop along the length of the tube showed that, in AEA tubes with larger angle θ values, pressure drop was more sensitive to changes in *Re*. An increase in angle θ also increased the pressure drop.

The results of the constituent terms of wall shear stress indicate that the velocity gradient term was several times greater than the effective viscosity term. This indicates that the most effective term in the wall shear stress equation is the velocity gradient term. Furthermore, the average wall shear stress along the length of the tube increased with an increase in angle θ.

A survey of the streamlines revealed that increasing angle θ from 60° to 80° caused the multi-longitudinal vortices to divide and increase in number from four to eight. On the other hand, increasing angle θ caused the cold fluid to impinge upon more paths near the hot fluid near the tube wall and increased the heat transfer.

Observation of the synergy between the velocity vector and temperature gradient indicated that the presence of multi-longitudinal vortices caused an increase in the angle between the velocity vector and temperature gradient, which increased heat transfer. It was observed that in Sections A, B and C, the number of areas with maximum dot products for the velocity vector and temperature gradient increased as angle θ increased. In addition, the two-dimensional equation of energy indicated that the most heat transfer occurred in the transition zone. Fluid flow also causes heat interaction along the tube because of the presence of reverse flows after the transition zone, which decreases heat transfer in the tube at a constant cross section. Calculation of the friction factor and average Nusselt number revealed that increasing angle θ increased both parameters.

Observation of the PEC values for all AEA tubes showed that the maximum PEC (1.09) was achieved at a low Reynolds number ($Re = 10{,}000$) in the AEA 90° tube. It was also observed that the PEC at $Re \geq 20{,}000$ has a number less than 1, which indicates that the use of this tube at $Re \geq 20{,}000$ is less economical than the circular tube.

References

1. Liu S, Sakr M (2013) A comprehensive review on passive heat transfer enhancements in pipe exchangers. Renew Sustain Energy Rev 19:64–81
2. Maiga SEB, Palm SJ, Nguyen CT, Roy G, Galanis N (2005) Heat transfer enhancement by using nanofluids in forced convection flows. Int J Heat Fluid Flow 26(4):530–546
3. Hassan H, Harmand S (2015) Effect of using nanofluids on the performance of rotating heat pipe. Appl Math Model 39(15):4445–4462
4. Gupta M, Kumar R, Arora N, Kumar S, Dilbagi N (2015) Experimental investigation of the convective heat transfer characteristics of TiO_2/distilled water nanofluids under constant heat flux boundary condition. J Braz Soc Mech Sci Eng 37(4):1347–1356
5. Mousavi SM, Farhadi M, Sedighi K (2016) Effect of non-uniform magnetic field on biomagnetic fluid flow in a 3D channel. Appl Math Model 40(15):7336–7348
6. Mokhtari M, Hariri S, Gerdroodbary MB, Yeganeh R (2017) Effect of non-uniform magnetic field on heat transfer of swirling ferrofluid flow inside tube with twisted tapes. Chem Eng Process 117:70–79
7. Soltanipour H, Khalilarya S, Motlagh SY, Mirzaee I (2017) The effect of position-dependent magnetic field on nanofluid forced convective heat transfer and entropy generation in a microchannel. J Braz Soc Mech Sci Eng 39(1):345–355
8. Habib MA, Mobarak AM, Attya AM, Aly AZ (1993) Enhanced heat transfer in channels with staggered fins of different spacings. Int J Heat Fluid Flow 14(2):185–190
9. Wang W, Bao Y, Wang Y (2015) Numerical investigation of a finned-tube heat exchanger with novel longitudinal vortex generators. Appl Therm Eng 86:27–34
10. Kundu B (2015) Beneficial design of unbaffled shell-and-tube heat exchangers for attachment of longitudinal fins with trapezoidal profile. Case Stud Therm Eng 5:104–112
11. Yang S, Zhang L, Xu H (2011) Experimental study on convective heat transfer and flow resistance characteristics of water flow in twisted elliptical tubes. Appl Therm Eng 31(14):2981–2991
12. Pozrikidis C (2015) Stokes flow through a twisted tube with square cross-section. Eur J Mech B 51:37–43
13. Zhao N, Yang J, Li H, Zhang Z, Li S (2016) Numerical investigations of laminar heat transfer and flow performance of Al_2O_3–water nanofluids in a flat tube. Int J Heat Mass Transf 92:268–282
14. Elsebay M, Elbadawy I, Shedid MH, Fatouh M (2016) Numerical resizing study of Al_2O_3 and CuO nanofluids in the flat tubes of a radiator. Appl Math Model 40(13):6437–6450
15. Guo ZY, Li DY, Wang BX (1998) A novel concept for convective heat transfer enhancement. Int J Heat Mass Transf 41(14):2221–2225
16. Li B, Feng B, He Y-L, Tao W-Q (2006) Experimental study on friction factor and numerical simulation on flow and heat transfer in an alternating elliptical axis tube. Appl Therm Eng 26(17):2336–2344
17. Meng J-A, Liang X-G, Chen Z-J, Li Z-X (2005) Experimental study on convective heat transfer in alternating elliptical axis tubes. Exp Thermal Fluid Sci 29(4):457–465
18. Chen W-L, Dung W-C (2008) Numerical study on heat transfer characteristics of double tube heat exchangers with alternating horizontal or vertical oval cross section pipes as inner tubes. Energy Convers Manag 49(6):1574–1583
19. Sajadi AR, Yamani Douzi Sorkhabi S, Ashtiani D, Kowsari F (2014) Experimental and numerical study on heat transfer and flow resistance of oil flow in alternating elliptical axis tubes. Int J Heat Mass Transf 77:124–130
20. White FM (1991) Viscous fluid flow, 2nd edn. McGraw-Hill, New York
21. Guo ZY (2003) A brief introduction to a novel heat-transfer enhancement heat exchanger. Internal report, Department of Engineering Mechanics, Key Laboratory for Thermal Science and Power Engineering of Ministry of Education, Tsinghua University, Beijing, China

22. Chen W-L, Guo Z, Co-K Chen (2004) A numerical study on the flow over a novel tube for heat-transfer enhancement with a linear Eddy-viscosity model. Int J Heat Mass Transf 47(14):3431–3439
23. Sajadi AR, Kowsary F, Bijarchi MA, Sorkhabi SYD (2016) Experimental and numerical study on heat transfer, flow resistance, and compactness of alternating flattened tubes. Appl Therm Eng 108:740–750
24. Launder BE, Spalding DB (1972) Lectures in mathematical models of turbulence. Academic Press, London
25. Van Doormaal JP, Raithby GD (1984) Enhancements of the SIMPLE method for predicting incompressible fluid flows. Numer Heat Transf 7(2):147–163
26. Chorin AJ (1968) Numerical solution of the Navier-Stokes equations. Math Comput 22(104):745–762
27. Versteeg HK, Malalasekera W (2007) An introduction to computational fluid dynamics: the finite method, 2nd edn. Pearson Education, London
28. Holmes DG, Connell SD (1989) Solution of the 2D Navier-Stokes equations on unstructured adaptive grids. In: 9th computational fluid dynamics conference. AIAA, p 1932
29. Rausch RD, Batina JT, Yang HTY (1991) Spatial adaption procedures on unstructured meshes for accurate unsteady aerodynamic flow computation. In: 32nd structures, structural dynamics, and materials conference. AIAA, p 1106
30. Warming RF, Beam RM (1976) Upwind second-order difference schemes and applications in aerodynamic flows. AIAA J 14(9):1241–1249
31. Launder BE, Spalding DB (1974) The numerical computation of turbulent flows. Comput Methods Appl Mech Eng 3(2):269–289
32. Petukhov BS, Irvine TF, Hartnett JP (1970) Advances in heat transfer. Academic Press, New York
33. Gnielinski V (1976) New equations for heat and mass-transfer in turbulent pipe and channel flow. Int Chem Eng 16(2):359–368 **(cited in [34])**
34. Bergman TL, Lavine AS, Incropera FP, Dewitt DP (2011) Fundamentals of heat and mass transfer, 7th edn. Wiley, New Jersey
35. Fluent A (2011) ANSYS FLUENT Theory Guide. ANSYS Inc., Canonsburg
36. Spalart PR, Shur M (1997) On the sensitization of turbulence models to rotation and curvature. Aerosp Sci Technol 1(5):297–302
37. Smirnov PE, Menter FR (2009) Sensitization of the SST turbulence model to rotation and curvature by applying the Spalart–Shur correction term. J Turbomach 131(4):041010
38. Çengel YA, Cimbala JM (2014) Fluid mechanics fundamentals and applications, 3rd edn. McGraw-Hill, New York
39. Tao W-Q, Guo Z-Y, Wang B-X (2002) Field synergy principle for enhancing convective heat transfer: its extension and numerical verifications. Int J Heat Mass Transf 45(18):3849–3856
40. Webb RL, Kim N-H (1994) Principles of enhanced heat transfer. Taylor Francis, New York